# Analysis of shear capacity of brittle lightweight concrete beams using interface elements

H.D. Basche, I. Rhee, K.J. Willam, B.P. Shing,
*University of Colorado at Boulder*

ABSTRACT: In this paper, the failure mechanisms of lightweight concrete beams without shear reinforcement are examined by means of nonlinear finite element analysis and experimental observations. For the 2-D computational simulations, discrete inter- and intra-element crack models using zero-thickness interface elements are used. The loss of cohesion is described in terms of a consistent damage formulation for mode I and mode II fracture. The objective is to capture the brittle failure under mixed mode fracture.

Keywords: Embedded cracks, Interface elements, shear capacity, All Lightweight Aggregate Concrete (ALWAC) Beams

## 1 Introduction

A challenging topic was and still is the determination of the failure behavior of concrete beams without shear reinforcement. The mechanism of shear failure is not entirely understood. Using new cement-based materials leads to the adoption of semi empirical formulas to evaluate the shear capacity of beams. Recent tests (Keller 2003) of 4-point-bending beams made of All Lightweight Aggregate Concrete (ALWAC) exhibited different failure behavior in comparison to common normal weight and normal strength concrete (NSC).

A single beam of the test series was selected for numerical evaluation using both intra- and interelement crack formulation with zero thickness interface. The theoretical failure load in bending is $V_{u,bend}$=142 kN and, hence almost two times higher than the experimental failure load, shown in Figure 1.

The main difference in the material behavior of these beams is the high brittleness of ALWAC, both in tension and compression. The beams did not fail after formation of an inclined crack, but there was a distinct increase of load capacity after the first peak, see Figure 1. The crack pattern of this beam is shown in Figure 2.

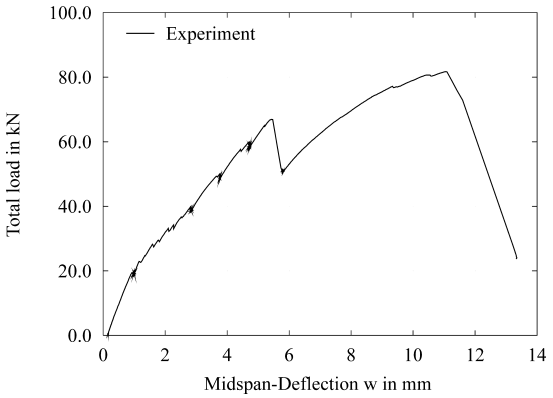


Figure 1. Experimental load-deflection curve

The weak tensile strength of concrete and the ensuing cracking is a major factor contributing to the nonlinearity of reinforced concrete structures. There are four major approaches for describing cracking in finite element analysis. They are (a) smeared (distributed) crack models, (b) embedded

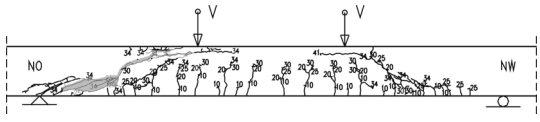


Figure 2. Crack pattern at failure

crack models, (c) discrete crack models, (d) fracture mechanics models. The inter-element crack formulation (c) is based on introduction of

additional elements (zero thickness interface elements) with finite stiffness for nonlinear behavior of concrete, i.e. for damage, between linear solid elements.

The intra-element formulation (b) is based on introduction of displacement discontinuities within a solid finite element. This formulation is also referred as embedded crack elements. In this case, occurrence of discrete cracks does not depend on element boundaries, but they are introduced within the element.

## 2 EXPERIMENTAL RESULTS AND MATERIAL PROPERTIES

### 2.1 *Shear beam*

Although several beams were tested in the test series by Keller (Keller 2003), only one beam with a single layer of reinforcement was numerically analyzed. The test setup and the position of the reinforcement is illustrated in Figure 3 and Figure 4, respectively. The beam was tested in deformation-control. Except for the overhang, there

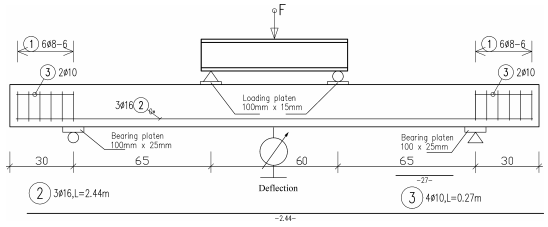


Figure 3. Static system and reinforcement

was no web reinforcement, within the span of $l$=1.90 m. The beam had a nominal shear slenderness ratio of $a/d$=4, whereby $a$ is the shear span and $d$ the effective depth. However, with the consideration of the dimension of the loading and

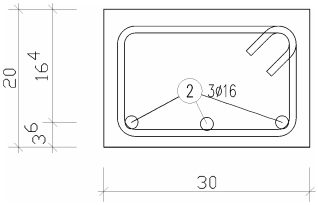


Figure 4. Cross section of beam SV6-2

bearing platen, the effective shear slenderness ratio reduces to $a/d$=3.35. The stress-strain behavior of ALWAC in uniaxial compression shows nearly linear behavior until the peak stress is reached, see Figure 5. The nonlinear inelastic strain at failure $\varepsilon_{pl}$ is only a fraction of that observed for NSC.

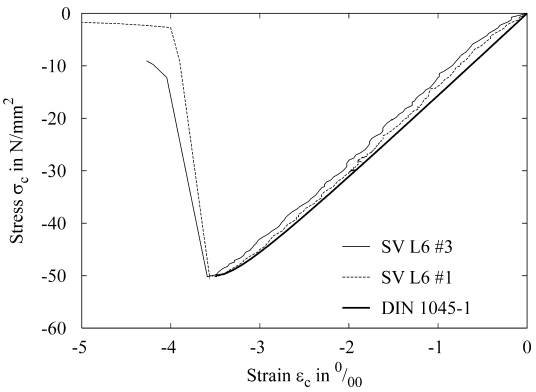


Figure 5. Stress-strain diagram of ALWAC in uniaxial compression

The ALWAC beam showed a fairly normal behavior: after formation of bending and shear cracks, one inclined shear crack propagated toward the loading platen. This corresponds to the first drop in the load-deflection curve shown in Figure 1. In contrary to the shear failure mode often observed, this diagonal crack did not lead to a loss of load bearing capacity in the form of crushing of the compression zone. Note the increase of 22 % of load bearing capacity beyond the large drop of strength due to shear cracking. Instead of penetrating the compression zone, the crack turned horizontally and propagated into a region underneath the loading platen. In fact, the compression zone above the neutral axis formed new cracks on the upper compressive fiber in the shear span, see Figure 2. The same behavior was observed in the tests of Dehn (Dehn 2001).

### 2.2 *Wedge Splitting Test and Mode I Fracture Energy*

For the determination of mode I fracture energy of ALWAC, wedge splitting tests were performed and numerically evaluated by means of FE analysis. For this computation, linear-elastic elements were used for the bulk with zero-thickness interface elements along the axis of symmetry, see Figure 6. In this case, it is sufficient to place interface-elements along the axis of symmetry because the experimental crack developed along a straight line from the notch to the bottom, see Figure 7.

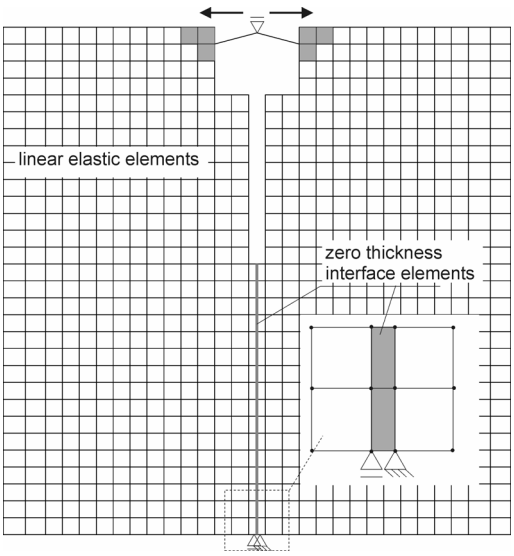


Figure 6. FE-mesh for simulation of wedge splitting tests

Figure 7. Crack formation in wedge splitting specimen

The normal interface tractions $t_n$ were computed from the normal interface displacements $u_n$ by the exponential function using the tensile uniaxial strength $f_t$ and the mode I fracture energy $G_f^I$

$$t_n = f_t \exp\left(-\frac{f_t \cdot u_n}{G_f^I}\right) , \qquad (1)$$

which is intended only for mode I fracture.

The numerically determined values for mode I fracture energy of the ALWAC were in the range of $G_f^I$=20 N/m to $G_f^I$=30 N/m. This leads to a good match of the experimental load-displacement curve. In comparison to NSC with fracture energy $G_f^I \geq 100$ N/m, this ALWAC exhibits a very brittle softening in tension, see Figure 8.

In this figure, the softening response of NSC and ALWAC having the same compressive strength are compared. For better illustration, the values of the tensile stress were normalized with regard to their different strength values in tension. This extreme brittleness requires special attention in the finite element formulation.

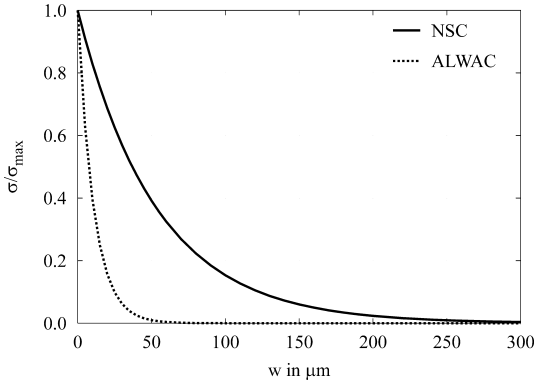


Figure 8. Comparison of tensile softening of NSC and ALWAC obtained numerically

## 3 SHEAR BEAM ANALYSIS WITH EMBEDDED DISCONTINUTY ELEMENTS

### 3.1 *FE-Discretisation*

The element used in this study was developed by Spencer&Shing (2001, 2003). It is based on a stress hybrid formulation which introduces a displacement discontinuity when the maximum principal stress reaches the tensile strength of concrete. According to the classification by Jirasek (Jirasek 1999), the element can be classified as a statically and kinematically optimal nonsymmetric (SKON) formulation.

At the beginning, the entire beam specimen was modeled to capture the effects of non-symmetric crack propagation. However, it was observed that neither the load-deflection curves nor crack propagation patterns showed any noticeable difference with the entire specimen or with the half specimen model. Hence, for the detailed study, only half of the beam was modeled as shown in Figure 9.

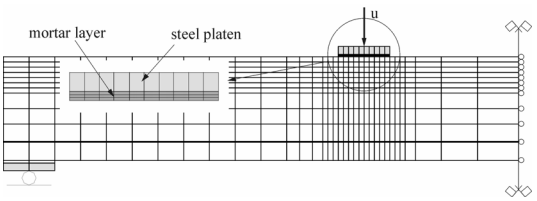


Figure 9. FE-Mesh with embedded cracks

The material properties of steel and lightweight concrete are summarized in Table 1.

Table 1. Material properties of ALWAC used for FE-analysis

| | E GPa | $f_c$ MPa | $G_f^I$ N/m | $G_f^{II}$ N/m |
|---|---|---|---|---|
| ALWAC | 14.2 | 56 | 11 | 11 |
| mortar | 30 | 50 | 30 | 300 |
| rebar | 195 | 530 | | |
| Load./bearing platen | 210 | 500 | | |

The reinforcement was modeled by truss elements without bending stiffness connected to the adjacent concrete elements by a zero-thickness bond interface element. The bond law followed the proposal by Mehlhorn (Mehlhorn 1985), with a limited shear bond strength.

Another important factor affecting the overall beam behavior was the proper discretization of the loading platen and the mortar between the steel platen and the top compressive fiber of the beam. The propagation of the shear crack in the horizontal direction underneath the loading platen leads to a complex stress and strain state in the compression zone. Besides the lateral constraint of the upper concrete fibers, there was a mismatch of the elastic modulus and Poisson's ratio between the steel and concrete leading to shear stresses in the contact zone causing the cracking of the mortar layer. Furthermore, the stresses $\sigma_{yy}$ and $\tau_{xy}$ cause splitting and delamination in the compression zone of the beam.

### 3.2 *Results*

Numerical tests showed that an improper discretization of the loading platen leads to unreasonable results due to unrealistic confinement effects in the compression zone in this area. For this reason, three layers of mortar elements were introduced, see Figure 9.

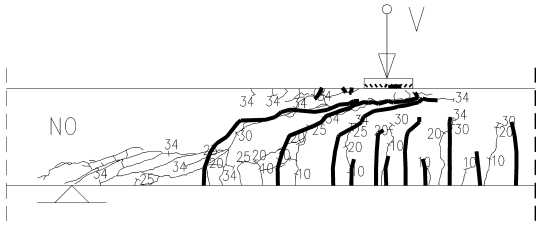


Figure 10. Comparison of numerical Cracks with experimental crack pattern

The plot of the numerical load-deflection curve with the experimental curve in Figure 11 shows very good agreement. The first peak load associated with shear cracking is well captured by the computation. The maximal load capacity of the test specimen could be reproduced although the loss of convergence in the numerical solution occurred slightly prematurely. The crack evolution given in Figure 10 matches the experimental crack pattern very well. Especially the horizontal crack agrees fully with the experimental observation and its occurrence corresponds to the drop in the load-deflection curve.

It should be noted that the postpeak response of the computation is very sensitive to the choice of material parameters and the solution scheme (step size, convergence criterion and iteration limiters).

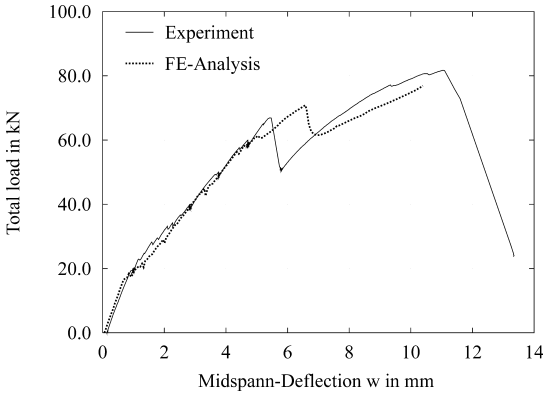


Figure 11. Comparison of experimental and computed load deflection curve

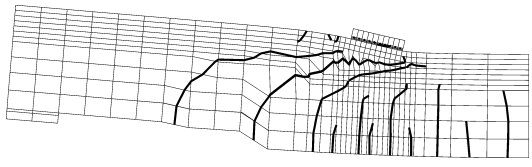

Figure 12. Deformed FE mesh with embedded cracks

## 4 COMPUTATION OF SHEAR BEAM WITH INTERFACE ELEMENTS

### 4.1 *Interfaces in concrete*

In discrete crack models, 'potential' cracks are spread over the FE mesh domain with zero-thickness interface elements that initially nearly enforce continuity of tractions and displacements across element boundaries. They are subjected to a mixed-mode failure criterion. Once the failure criterion is satisfied, 'potential' crack candidates can open or slide following the governing softening law.

For problems that involve a few dominants cracks, discrete interfaces provide a practical representation of the problem. In addition, aggregate interlock and bond slip in mono- and bi-materials can be represented by this discrete crack model although these physical issues are more related to topology. The viewpoint of the discrete crack models is still macroscopic in principle, with the basic behavior characteristics lumped in the elements. Therefore, an interface element has a life of its own in the elastic body. With cracking passing along element boundaries, the use of simplex elements such as the constant strain triangular (CST) element is well suited from a conceptual point of view as well as from the application standpoint shown in Figure 13. However, these simplex elements do not accommodate sharp strain gradients except with a very fine mesh. The stresses in the vicinity of the crack tip are mesh-dependent because of the large stress concentration in its neighborhood.

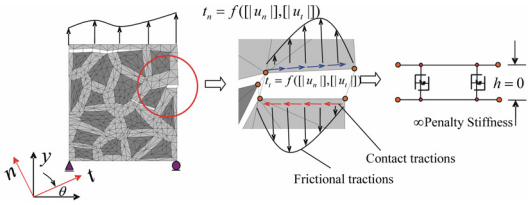


Figure 13. Description of the four noded interface element in two dimension

### 4.2 *Cohesive interface material law*

The material separation and thus localized damage of the structure is described by cohesive interface elements. Thereby, adjacent continuum elements are not damaged in this approach. Using this technique, the behavior of the material is split into two parts, the damage-free continuum with elastic material behavior that can vary across the body, and the interspersed cohesive interface zones between continuum elements, which represent localized damage of the material. The interface elements open up when damage occurs and entirely loose their stiffness at failure so that neighboring continuum elements are disconnected. For this reason, the crack can propagate only along the boundaries of solid elements in the form of interelement failure. If the crack propagation direction is not known in advance, the mesh generation has to be sufficiently refined such that different crack interface paths are possible. The separation of the cohesive interfaces is calculated from the displacement jump $[|\mathbf{u}|]$, i.e. the difference between the displacements in adjacent continuum elements,

$$[|\mathbf{u}|] = \mathbf{u}^{+} - \mathbf{u}^{-}$$
$$[|u|] = \sqrt{[|u|]_n^2 + \alpha[|u|]_t^2} \tag{2}$$

More common than the definition of the separation vector in global coordinates is the description in a local coordinate system, namely the distinction between normal separation, $[|u|]_n$, and tangential slip, $[|u|]_t$ in Eq. (2). The critical separation is denoted as $[|u|]_0$, and $[|u|]_f$ is defined by Figure 14. The maximum traction $T_0$, is used as a fracture parameter, which is designated as 'cohesive strength' and is the value of the traction at $[|u|]_0$. The value of $T_0$ describes the maximum value of the traction separation relation $T([|u|])$. In the following, we use the exponential cohesive law in Eq. (3), which is shown in Figure 14.

$$T([|u|]) = T_o \exp^{\beta\left(1-\frac{[|u|]}{[|u|]_o}\right)} \tag{3}$$

where $\beta = \dfrac{[|u|]_o}{[|u|]_f - [|u|]_o}$

Considering failure due to simultaneous normal and shear tractions, one has to introduce a new interaction quantity for damage hypothesis. As mentioned before, failure occurs in pure tensile cracking when the separation exceeds the maximum separation $[|u|]_o$. Under combined normal and shear failure in the cohesive element, the failure hypothesis contains a normal and a shear component, see Eq. (2). In this case, the shear damage will reduce the strength in the normal direction and vice versa. The factor $\alpha$ in Eq. (2) ranges between 0 and 1.

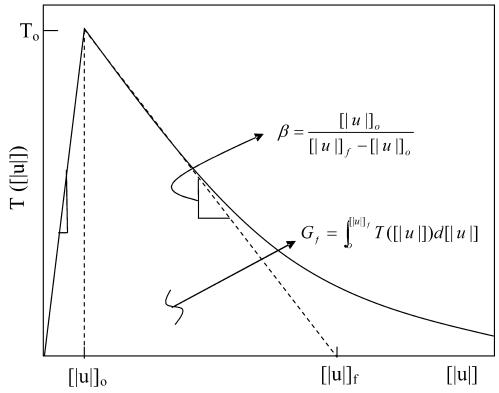


Figure 14. Softening law for interfaces

The competing normal and tangential separation effects are used to define the interaction relation of shear and normal separation, shown in Figure 15.

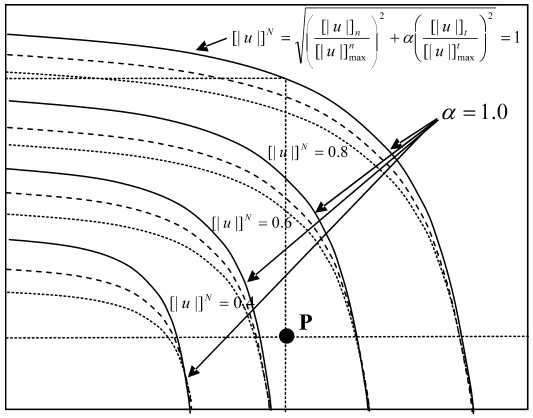


Figure 15. Interaction between normal separation and tangential slip

## 4.3 *Finite element modeling*

In spite of the disadvantage of the non-adaptive method of defining cracks and the lack of generality in possible crack directions, a structured mesh, like the 'union jack' type was being used for the sake of simplicity. Therefore, the possible crack directions are limited for horizontal, vertical and ±45-degree diagonal directions. A total of 8,240 nodes (16,840 dofs) and 6918 elements (CST: 2,830, INT2D: 4,088) are used for the mesh in Figure 16. The dimension and material parameters of SV6-2 are the same as shown in Figure 3, Figure 4 and Table 1, respectively. Elastic CST elements were used for concrete itself at the macro level. Two different interface types are defined to illustrate the nonlinearities of reinforced concrete. They are concrete-concrete interfaces (C-C) and concrete-steel interfaces (C-S). The former is introduced to capture the softening behavior of plain concrete due to tensile cracking or compression failure due to slippage at inclined boundaries of the triangles. The latter is known as 'bond slip' interface conditions which mainly affect the crack spacing of flexural cracks in the middle of beam span in accordance with the slip-shear relation. This relation depends upon the mechanical and chemical bonds in C-S interfaces.
The horizontal reinforcement was modeled by CST elastic triangles in order to take dowel action into account. In addition, bar elements were also used for the horizontal reinforcement in order to compare the effect of the reinforcement model on the global load-deflection curve as well as the deformed (cracked) state of beam.

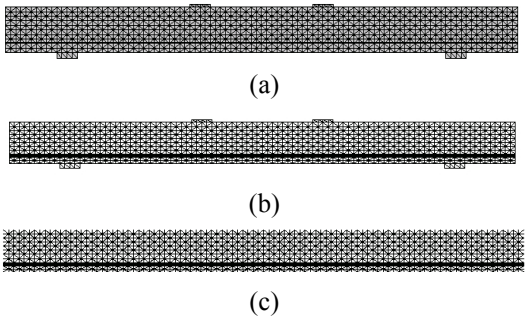


Figure 16. Basic mesh layouts of elastic CST triangles, four noded interface elements along each triangle: (a) two-noded bar elements connected by C-S interface, (b) beam elements which consist of CST triangles, (c) four node C-C, C-S interfaces lines

## 4.4 *Results and discussions*

The main results are shown through Figure 17 to Figure 19. The main shortcoming of this uni-axial traction vs. separation law in Eqs. (2) and (3) is the modelling of the compression behavior of interfaces. Normally, the interfaces remain intact in compression so that the compressive stress in adjacent concrete elements is transferred linear elastically if only compression forces are acting perpendicular to the interfaces (crack closure effect). However, due to the combination of normal and tangential interface stresses (at inclined interface elements), the compression failure of a beam may develop prematurely in spite of the fact that the compression strength of concrete is not yet reached. Especially, in the SV6-2 beam, the thin compression top layer resisted compression failure up to the load level at which global failure occurs. For this reason, the top element layers of the beam in Figure 16 are defined by a factor $\alpha$=0.01 in Eq. (2) while for the rest of the beam, $\alpha$=1 is used in order to avoid the premature compression failure

in the top element layers. The main difference between the two simulations using axial bars and beams with bending and shear resistance for the reinforcement is the appearance of horizontal 'peel-off' cracks shortly after diagonal shear cracks localize. This is known as dowel action of the reinforcement. The other observation is that numerical difficulties arise in the case of the bar-reinforced beam shortly after the major shear crack develops near support in Figure 17 and Figure 19. However, in case of beam-reinforcement, the numerical difficulties are delayed because of the enhanced rotational bending stiffness. This nonzero bending stiffness stabilizes the response near the inflection point of the deflected shape. More sophisticated solvers such as arc-length method, etc. should be used for this type of analysis. In Figure 17 and Figure 18, the deformed mesh of the cracking mode of the damaged beam does not show symmetry. This loss of symmetry is caused by numerical imperfections for seeking a properly converged state of the solution. Figure 19 shows that the initial stiffness of the reinforcement using beam elements is higher than the experimental result which may be partly caused by the undue stiffness enhancement of using CST-triangles which were highly skewed for modeling the reinforcement.

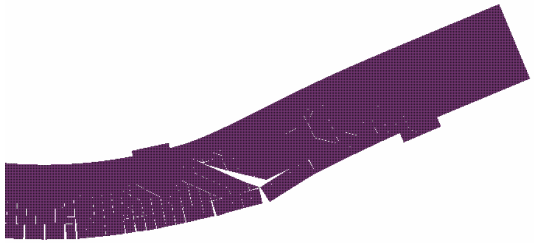

Figure 17. Crack patterns of SV6-2 using two nodded bar elements for horizontal reinforcement. . (Magnification = 30.0)

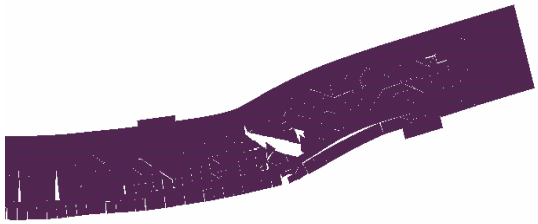

Figure 18. Crack patterns of SV6-2 using beam elements (consist of CST triangles) for horizontal reinforcement. (Magnification = 30.0)

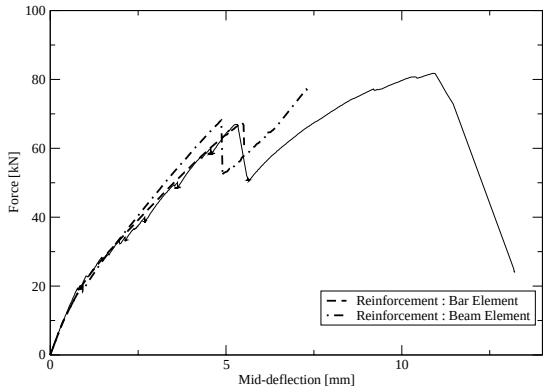


## 5 MODEL FOR POSTPEAK BEHAVIOR

Usually, a distinct postpeak increase after the formation of an inclined crack is expected in prestressed concrete beams. The postpeak bearing mechanism of prestressed beams is often explained by a lattice model which may be extended to model non-prestressed beams. However, in adapting this model to non-prestressed ALWAC beams with postpeak behavior, some shortcomings should be discussed. One objective of the numerical examination was to look behind this mechanism and to find a possible explanation for the postpeak load increase.

The deformed computational mesh as well as the experimental observations showed an inflection point for curvature in the upper compressive fiber. This kink cannot be explained by means of a lattice model but rather by a system of three rigid bodies, see Figure 20. The remaining compression zone is between the rigid bodies and forms a 'secondary' beam. This explains both (i) the deformed shape of the beam, see Figure 21, and (ii) the occurrence of the tensile cracks in the compression zone. The foregoing midspan deflection is caused by the moment introduced by the 'secondary' beam.

This model also explains the increase of postpeak load by top reinforcement. Usually the influence of a compressive reinforcement on the shear capacity is negligible. But the test data clearly showed (Keller 2003) that the top reinforcement significantly increases the post peak-load capacity. In this case, the top reinforcement strengthened the 'secondary' beam acting as tensile reinforcement.

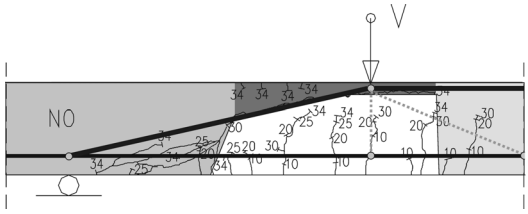


Figure 20. System of rigid bodies (gray shaded) and lattice model

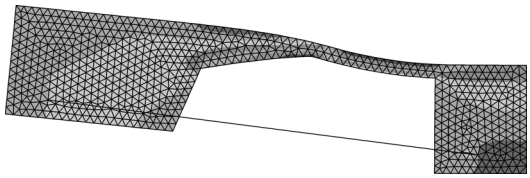

Figure 21. Stress and deformation of linear-elastic model

## 6 CONCLUSIONS

The investigation using two FE-analysis approaches captured the main features of progressive failure in ALWAC beams without transverse shear reinforcement. Additional research is required to examine the large rotation aspects of shear failure.

## 7 ACKNOWLEDGEMENTS

The work of the lead author was supported by a fellowship within the Postdoc-Programme of the German Academic Exchange Service (DAAD). The other authors wish to acknowledge partial support of this research by the National Science Foundation under grant CMS-0084598.

## 8 REFERENCES

Dehn, F. 2001: Einflussgrößen auf die Querkrafttragfähigkeit schubunbewehrter Bauteile aus konstruktivem Leichtbeton, Universität Leipzig, Diss.

Jirasek, M. 1999. Comparative study on finite elements with embedded discontinuities. In: Computer Methods in Applied Mechanics

Keller, C. 2003. Abschlussbericht zum DFG-Forschungsvorhaben: Schubtragverhalten vorgespannter Leichtbetonbalken, University of Leipzig

Mehlhorn, G. & Keuser, M. 1985. Isoparametric Contact Elements for Analysis of Reinforced Concrete. In: Me, C. (Hrsg.) ; Okamurayer, H. (Hrsg.): Finite Element Analysis of Reinforced Concrete Structures, 1985, Tokyo, ASCE

Spencer, B. W. 2002. Finite Elements with Embedded Discontinuities for Modeling Reinforced Concrete Members, University of Colorado at Boulder, PhD-thesis

Spencer, B.W. & Shing, P.B. 2003, Rigid-Plastic Interface for an Embedded Crack, International Journal for Numerical Methods in Engineering, Vol. 56, 2163-2182

Spencer, B. and Shing, P.B. 2001, Stress Hybrid Embedded Crack Element for Analysis of Concrete Fracture, in Finite Element Analysis of Reinforced Concrete Structures, Special Publication SP-205, American Concrete Institute, 323-345

Willam, K. et al. 2003, Interface Damage Model for Thermomechanical Degradation of Heterogeneous Materials, in press in Special WCCMV Issue on Computational Failure Mechanics, CMAME